

Geometric and compositional factors on critical current density in $\text{YBa}_2\text{Cu}_3\text{O}_{7-\delta}$ films containing nanorods

Tomoya Horide¹ , Sho Nagao¹, Ryosuke Izutsu¹, Manabu Ishimaru¹, Ryusuke Kita² and Kaname Matsumoto¹

¹ Department of Materials Science and Engineering, Kyushu Institute of Technology, 1-1 Sensui-cho, Tobata-ku, Kitakyushu 804-8550, Japan

² Graduate School of Integrated Science and Technology, Shizuoka University, 3-5-1, Johoku, Naka-ku, Hamamatsu 432-8561, Japan

E-mail: horide@post.matsc.kyutech.ac.jp

Received 23 January 2018, revised 30 March 2018

Accepted for publication 16 April 2018

Published 11 May 2018



Abstract

Critical current density (J_c) was investigated in $\text{YBa}_2\text{Cu}_3\text{O}_{7-\delta}$ films containing nanorods prepared with various nanorod materials, with variation of nanorod content, substrate temperature, and oxidization condition. Three types of compositional situation were realized: films containing strain induced oxygen vacancies; fully oxidized films containing cation compositional deviation; and oxygen deficient films. Normalized J_c – B behavior was determined via the matching field, which is a geometric factor, regardless of the compositional details. A J_c –critical temperature (T_c) relation depending on distribution and fraction of compositional deviation (cation compositional deviation and strain induced oxygen vacancies) was found: the J_c values decreased with decreasing T_c due to the effect of T_c on nanorod pinning strength in the fully oxidized films; J_c decreased with decreasing oxygen pressure in the film cooling process after film deposition in spite of T_c remaining almost the same, due to reduction of the effective area for current flow in the oxygen deficient films. Thus, a J_c landscape based on geometric and compositional factors was obtained. The study highlights the importance of the J_c – T_c analysis in the understanding of J_c in $\text{YBa}_2\text{Cu}_3\text{O}_{7-\delta}$ films containing nanorods.

Keywords: critical current, YBCO, film, nanorod

(Some figures may appear in colour only in the online journal)

1. Introduction

Vortex pinning is an important matter in the application of superconducting wires and tapes [1] and the fundamental understanding of superconducting properties [2]. Various pinning centers have been experimentally and theoretically investigated in metallic, cuprate, and Fe based superconductors. Nanocomposite structure comprising nanorods and nanoparticles significantly improves critical current density (J_c) in $\text{YBa}_2\text{Cu}_3\text{O}_{7-\delta}$ (YBCO) films [3–5], and the pinning mechanism of BaMO_3 (BMO, M = Zr, Sn, Hf etc) nanorods should be understood for further control of J_c in YBCO nanocomposite films.

The nanorods work as c -axis correlated pinning centers to significantly improve the J_c for magnetic field parallel to the c -axis [3, 6–11]. Selection of nanorod materials and optimization of fabrication conditions resulted in very high J_c [7, 12]. The influence of nanorod density [13], nanorod length [14], and nanorod diameter [15] on vortex pinning has been discussed based on magnetic field and field angle dependences of J_c : the nanorod length and density are dominant to J_c , but the nanorod diameter does not affect the J_c . In addition to these geometric factors, critical temperature (T_c) in bulk YBCO depends on oxygen content ($\delta = 0$ –1) [16], indicating that composition of YBCO is another important factor for the J_c values. The oxygen non-stoichiometry leads to a

Table 1. Summary of samples. * B_{Φ} is the same as the B_{Φ} in BHO(4.7, 880) since the cooling process does not affect nanorod geometry.

Sample	P_{O_2} during cooling	Thickness (nm)	$T_{c,0}$ (K)	J_c at 77 K, 0 T (MA cm ⁻²)	B_{Φ} from T_{irr} - B (T)
YBCO+BZO(4.1, 870)	55 000 Pa	200	89.0	1.7	3
YBCO+BZO(4.1, 880)	55 000 Pa	150	89.4	1.6	2
YBCO+BZO(4.1, 890)	55 000 Pa	190	89.9	2.5	2
YBCO+BZO(8.2, 870)	55 000 Pa	160	79.1	0.32	—
YBCO+BZO(8.2, 880)	55 000 Pa	170	85.0	0.50	6
YBCO+BZO(8.2, 890)	55 000 Pa	140	88.2	0.74	2
YBCO+BSO(3.6, 880)	55 000 Pa	180	90.6	3.1	1.2
YBCO+BSO(3.6, 890)	55 000 Pa	150	90.4	3.5	1
YBCO+BHO(4.7, 870)	55 000 Pa	160	84.1	0.91	6
YBCO+BHO(4.7, 880)	55 000 Pa	160	87.6	1.2	5
YBCO+BHO(4.7, 890)	55 000 Pa	190	87.0	0.43	4
YBCO+BSO(5.4) [15] ^a	55 000 Pa	220	89.6	1.9	2
YBCO+BHO(4.7, 880)-OD1	5000 Pa	160	85.8	0.68	*
YBCO+BHO(4.7, 880)-OD2	500 Pa	160	87.3	0.052	*

^a BSO(5.4) has already been reported in [15].

characteristic structure of interface and matrix in YBCO+BMO films: the nanorod/matrix interface contains a high concentration of oxygen vacancies due to strain [17]; the strain originating from the interface increases the concentration of oxygen vacancies in the YBCO matrix, resulting in T_c degradation [18]. The composition of YBCO films may also exhibit deviation of cations, depending on deposition conditions [19]. The J_c values in the YBCO+BMO films are affected by compositional situations of this kind, but the J_c in YBCO+BMO films has previously been discussed based on the nanorod structure, without considering the effects of composition. Thus, although some work has been directed toward the analysis of the influence of oxygen non-stoichiometry on structure and T_c in YBCO+BMO films, the influence of the compositional situation on J_c has not yet been made clear.

In the present paper, the influence of the compositional situation on J_c in YBCO+BMO films is investigated. The geometric effect—namely, nanorod density—is fixed, and a J_c - T_c relation is sought, to clarify the role of compositional factors in determining J_c . Based on the results, the compositional and geometric factors are discussed separately, to explain the J_c mechanism in YBCO+BMO films.

2. Experimental

YBCO+BMO films were fabricated using pulsed laser deposition (PLD), in which the BMO materials (BaZrO₃ (BZO), BaSnO₃ (BSO), BaHfO₃ (BHO)), BMO content in the mixed targets (3.6–8.2 vol%) and substrate temperature (870 °C, 880 °C, 890 °C) were varied. After the deposition, the films were cooled down to room temperature in an oxygen atmosphere over ~1 h. The oxygen pressure (P_{O_2}) was set to 55 000 Pa for fully oxidized films, while P_{O_2} was set to 5000 Pa and 500 Pa to prepare oxygen deficient YBCO+BHO(4.7, 880) films. Here, YBCO+BMO(x , y) denotes an YBCO+BMO film prepared at y °C using the YBCO+BMO(x vol%) target. The

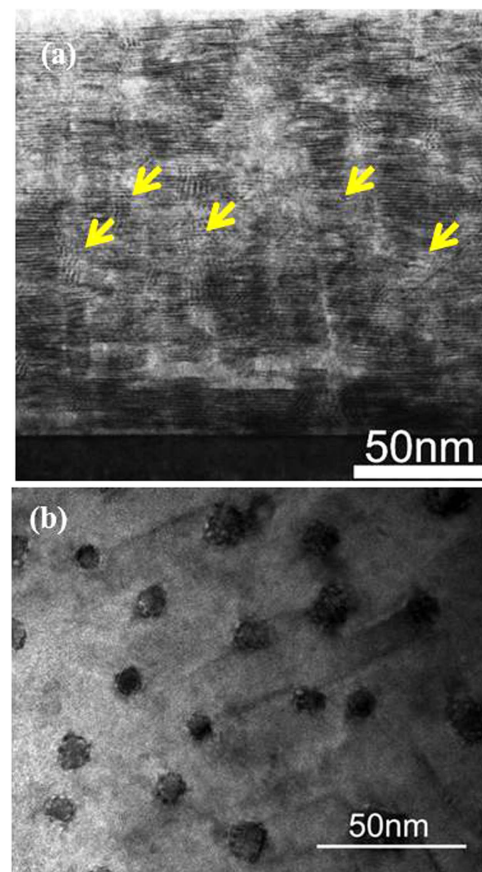


Figure 1. (a) Cross-sectional TEM image of the fully oxidized YBCO+BHO(4.7, 870). Arrows show the nanorods. (b) Plane-view TEM image of the fully oxidized YBCO+BSO(3.6, 880).

thickness was fixed at 130–200 nm. Table 1 is a list of the films prepared in the present study. The c -axis length was evaluated using x-ray diffraction (XRD), and the nanostructure was observed using transmission electron microscopy (TEM). T_c , J_c , and irreversibility temperature (T_{irr}) were measured using the Physical Property Measurement System. The electric field

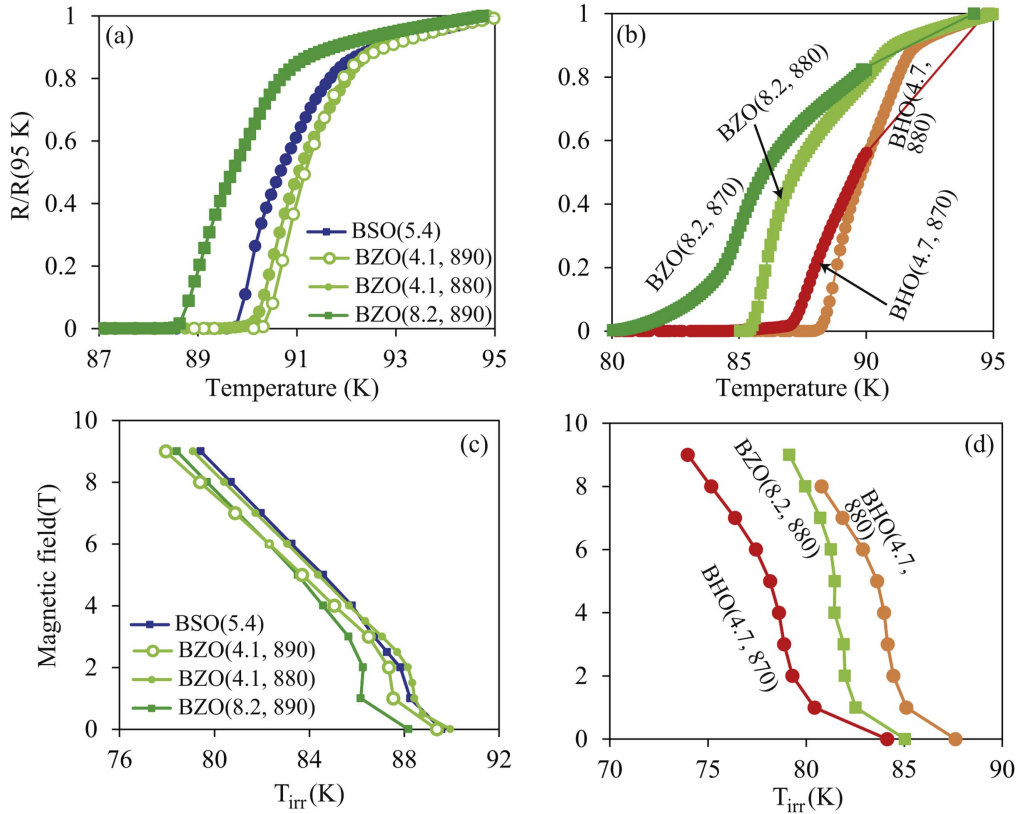


Figure 2. $R/R(95\text{ K})$ – T curves in fully oxidized films with $B_{\Phi} = 2\text{ T}$ (a) and $B_{\Phi} = 5\text{--}6\text{ T}$ (b). T_{irr} – B (magnetic field) curves in fully oxidized films with $B_{\Phi} = 2\text{ T}$ (c) and $B_{\Phi} = 5\text{--}6\text{ T}$ (d).

criterion was $1\text{ }\mu\text{V cm}^{-1}$ for T_{irr} and T_c zero($T_{c,0}$), and $10\text{ }\mu\text{V cm}^{-1}$ for J_c .

3. Results

Figure 1 shows a bright field cross-sectional TEM image of the YBCO+BHO(4.7, 870) and a plane-view TEM image of the YBCO+BSO(3.6, 880). The diameter of nanorods is $\sim 6\text{ nm}$ for the YBCO+BHO(4.7, 870), and the nanorod density and nanorod diameter are $9.3 \times 10^{14}\text{ m}^{-2}$ and $\sim 10\text{ nm}$ for the YBCO+BSO(3.6, 880).

Figures 2(a) and (b) show the temperature dependence of resistance in the films. Some films with large BMO content exhibited a two-step transition. Figures 2(c) and (d) show the T_{irr} – B curves in the films. T_{irr} – B curves exhibit a shoulder at $\sim B_{\Phi}$ ($=n\phi_0$, where n is the nanorod density and ϕ_0 is the flux quantum) in a YBCO containing c -axis correlated pinning centers [13]. The T_{irr} – B shoulder was observed in the present films, and B_{Φ} was estimated from the T_{irr} shoulder. Table 1 summarizes $T_{c,0}$ and matching field (B_{Φ}) in the films. The B_{Φ} values in the TEM (1.9 T) and T_{irr} – B (1.2 T) are not so significantly different in the YBCO+BSO(3.6, 880). $B_{\Phi} = 1\text{--}6\text{ T}$ depending on BMO selection, BMO content, and substrate temperature, and B_{Φ} decreased with increasing substrate temperature. Heavy doping of BMO may increase the nanorod diameter [13] at high temperature, which reduces B_{Φ} in a constant volume fraction of BMO. As

a result of this sensitive variation of structure, B_{Φ} showed significant dependence on substrate temperature in the case of large BMO content, especially in the YBCO+BZO(8.2). We selected the films with $B_{\Phi} = 2\text{ T}$ and $B_{\Phi} = 5\text{--}6\text{ T}$ to fix the matching field, i.e. the geometric factor. In addition to the present films, the previously reported YBCO+BSO(5.4) film [15] is also discussed in this paper. In films with $B_{\Phi} = 2\text{ T}$, the shoulder is observed at 2 T and almost the same T_{irr} – B behavior is observed regardless of $T_{c,0}$ values (88–90 K). Similar results were obtained for $B_{\Phi} = 5\text{--}6\text{ T}$ ($T_{c,0} = 84\text{--}88\text{ K}$).

Figures 3(a) and (b) show the magnetic field dependence of J_c and $J_c/J_c(0\text{ T})$ at 77 K for $B_{\Phi} = 2\text{ T}$. Similar $J_c/J_c(0\text{ T})$ behavior was obtained, although the J_c values are different. Figure 3 shows the magnetic field dependence of global pinning force, $F_p(=J_cB)$ at 77 K, in fully oxidized films with $B_{\Phi} = 2\text{ T}$. Figure 3(d) also shows the $F_p/F_{p,\text{max}}$ – B curves, where $F_{p,\text{max}}$ is the maximum of F_p . An F_p peak is observed at 2–3 T, due to the matching field effect [20, 21]. Figure 3 indicates that the $J_c/J_c(0\text{ T})$ – B and $F_p/F_{p,\text{max}}$ – B behavior do not depend on films, although the J_c values are different among the films. To address F_p – B behavior at low temperature, figure 4(a) shows the F_p – B curves at 40 K. At 40 K, the F_p – B behavior changes at $\sim 3\text{ T}$: the F_p does not depend so strongly on magnetic field for magnetic fields higher than 3 T. Also at 40 K, similar F_p – B behavior was obtained for $B_{\Phi} = 2\text{ T}$, although the J_c values were different. To discuss the difference in J_c values, figure 4(b) shows J_c as a function

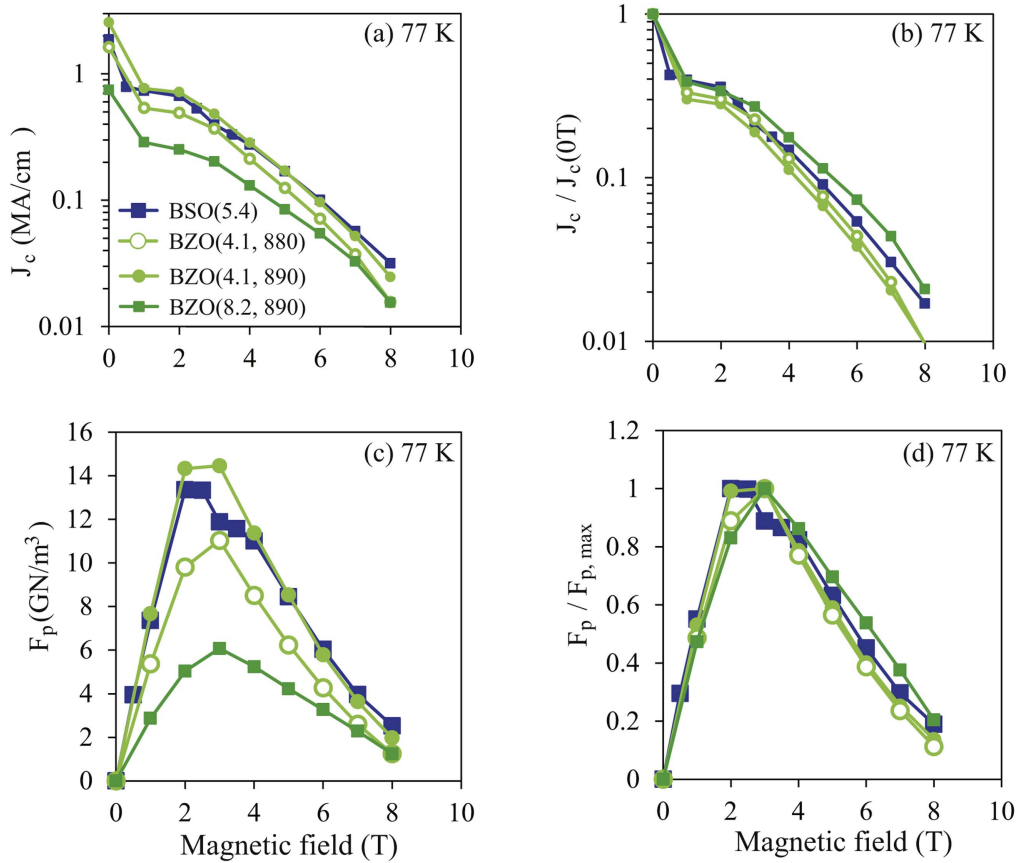


Figure 3. Magnetic field dependence of (a) J_c and (b) $J_c/J_c(0\text{ T})$ at 77 K in fully oxidized films with $B_\Phi = 2$ T. Magnetic field dependence of (c) F_p and (d) $F_p/F_{p,\text{max}}$ in fully oxidized films with $B_\Phi = 2$ T at a temperature of 77 K. The J_c in the YBCO+BSO(5.4) [15] were redefined at the same J_c criterion as the present films. In (a)–(d), the same symbols are used to represent the same samples.

of $T_{c,0}$ at 77 K, 65 K, and 40 K in a magnetic field of 5 T. J_c decreases with decrease in $T_{c,0}$ regardless of nanorod fabrication condition, showing that the J_c strongly depends on $T_{c,0}$ when the matching field is the same.

Figures 5(a) and (b) show the magnetic field dependence of J_c and $J_c/J_c(0\text{ T})$ for $B_\Phi = 5$ –6 T. Although the $T_{\text{irr}}-B$ curve in YBCO+BZO(8.2, 870) is not shown in figure 2(d), the $J_c/J_c(0\text{ T})-B$ curve at 65 K is similar to those of other films with $B_\Phi = 5$ –6 T. We have previously demonstrated that the normalized J_c-B behavior was determined by B_Φ [13], and the J_c-B behavior is almost the same for $B_\Phi = 2$ T in figure 3. The $J_c/J_c(0\text{ T})-B$ curves in figure 5(b) suggest $B_\Phi \sim 5$ –6 T also in YBCO+BZO(8.2, 870). Figure 5 shows the magnetic field dependence of F_p at 40 K and 65 K for $B_\Phi = 5$ –6 T. The matching field in the YBCO+BZO(8.2, 870), YBCO+BZO(8.2, 880), and YBCO+BHO(4.7, 870), and YBCO+BHO(4.7, 880) is ~ 5 –6 T. For the oxygen deficient YBCO+BHO(4.7, 880)-OD1 film, a F_p peak is at 6–8 T for 65 K and at >7 T for 40 K. Although the F_p-B behavior is slightly different due to a slight difference in B_Φ , similar F_p-B behavior is observed for $B_\Phi = 5$ –6 T, but the J_c values differ between the films. The F_p peaks are observed at 4 T in the OD2 film in figure 5. The conditions at the deposition which are the most dominant to the nanorod geometry are the same in BHO(4.7, 880), OD1, and OD2. It is

considered that the significantly oxygen deficient situation (very low J_c) altered the pinning situation with respect to the nanorod pinning strength and random pinning, and thereby the magnetic field dependence of J_c . However, it is apparent that the J_c in OD2 is significantly small compared with the other samples with large oxygen content. Even if it is compared with that in the BHO(4.7, 890) with $B_\Phi = 4$ T, the conclusion on the influence of oxygen content on J_c , which will be discussed in figure 6, is not altered.

Figures 6(a) and (b) compare the $J_c-T_{c,0}$ relation at 3 T for the films of figures 3 and 5; three types of $J_c-T_{c,0}$ relation were obtained for (A) the fully oxidized films ($B_\Phi = 2$ T, figures 3, 4); (B) the fully oxidized films ($B_\Phi = 5$ –6 T, figure 5); (C) the oxygen deficient films ($B_\Phi = 5$ –6 T, figure 5). In figures 6(a) and (b), J_c decreased with decrease in $T_{c,0}$ in both series A and B, but more rapidly in series A. Both series A and B contain well-defined nanorods, and geometric degradation of nanorods was not observed even at 870 °C, as shown in figure 1. As shown in the $R-T$ curves in figure 2, some films with $B_\Phi = 5$ –6 T (series B) exhibited a two-step superconducting transition. The series B films with the two-step transition consisted of strong and weak superconducting regions, and the weak superconducting region degraded $T_{c,0}$. Whereas $T_{c,0} \sim T_{c,\text{str}}$ (T_c of the strong superconducting region) in the case of the sharp transition, the $T_{c,0}$ for the two-step transition

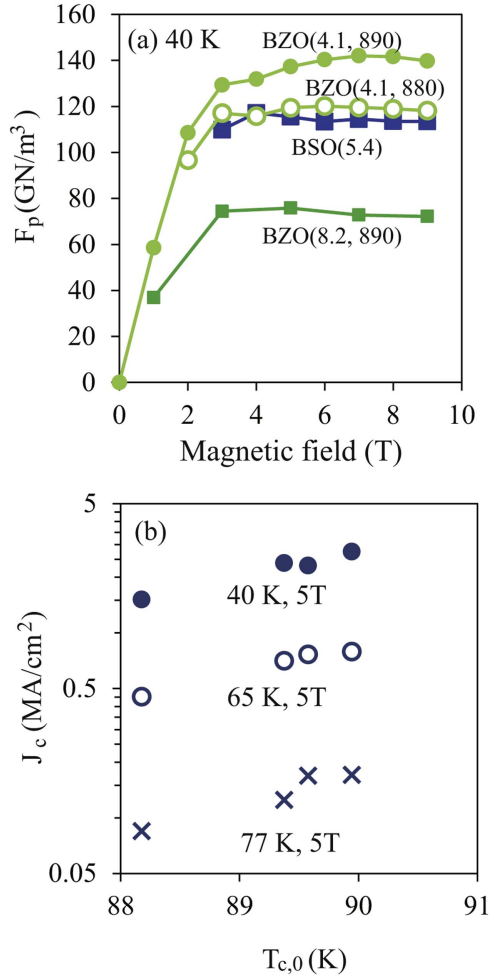


Figure 4. (a) Magnetic field dependence of F_p in the fully oxidized films with $B_\phi = 2$ T in a temperature of 40 K. (b) $T_{c,0}$ dependence of J_c at 77 K, 65 K, and 40 K in a magnetic field of 5 T.

is determined by the weak superconducting regions, which form a percolation network. To exclude the effect of the two-step transition, $T_{c, \text{str}}$ was estimated by extrapolating the $R-T$ curves at $R/R(95 \text{ K}) = 0.2-0.5$ to $R = 0$. The $J_c-T_{c, \text{str}}$ relation in series B approaches the $J_c-T_{c,0}$ relation in series A, suggesting that the strong superconducting region affected J_c more dominantly in series B. The J_c decrease with T_c is reasonable because T_c determines the order parameter and the nanorod pinning strength. Similar J_c decrease has been observed in oxygen reduced YBCO tapes without artificial pinning centers in the underdoped region [22].

4. Discussion

The geometric factors influencing J_c , such as matching field effect, are relatively well known. Here, the effects of composition on J_c in addition to the geometric factors are discussed in detail, to deepen the understanding of the J_c factors in the present films.

4.1. Geometric factor (matching field)

The F_p peak was observed at $\sim B_\phi$ at temperatures of 77 K and 65 K in the present films. On the other hand, dual peak behavior in F_p-B curves has been observed in YBCO+BZO films, owing to two types of pinning contribution [23]. The difference between the present films and [23] originates from the geometric attributes of nanorods, especially B_ϕ . In the case of small B_ϕ , the pinning effect of nanorods is relatively weak, maybe resulting in a dual F_p-B peak. In the present films with $B_\phi = 2$ T, the F_p at high magnetic field ($> B_\phi$) is nearly equal to the F_p at B_ϕ at 40 K, resulting in the disappearance of the clear F_p peak. Thus, the F_p-B behavior is strongly affected by the relative strength of nanorod pinning, to which both the geometric factor and the pinning strength are dominant. Although the observation of the F_p peak at B_ϕ depended on B_ϕ and temperature, characteristic behavior in F_p-B (crossover, peak) was observed both in the present study and [23], showing that B_ϕ is an important factor in describing the F_p-B behavior.

4.2. Compositional situation of films

To discuss the various compositional situations, $T_{c,0}$ as a function of the c -axis length is shown in figure 7, where the c -axis length dependence of $T_{c,0}$ for the strain induced oxygen vacancy (SIOV) [18] and oxygen deficient YBCO [16] is compared with the present results. For the SIOV, oxygen vacancy formation energy (E_{OV}) as a function of the c -axis length ($E_{OV}-c$) was calculated using the density functional theory calculation. δ as a function of the c -axis length ($\delta-c$) was obtained from the relation of $\delta \sim \exp(-E_{OV}/kT)$ and $E_{OV}-c$, where k is the Boltzmann constant and $T = 400^\circ \text{C}$ [18]. From the $\delta-c$ and $T_c-\delta$ relations experimentally obtained in bulk YBCO [16], the T_c was obtained as a function of c -axis length. According to the density functional theory calculation [19], the tensile strain in the YBCO matrix from nanorods reduces the E_{OV} . On the other hand, for oxygen deficient YBCO, T_c was determined from the $T_c-\delta$ relation experimentally obtained in bulk YBCO [16]. In both cases, oxygen content and T_c decreased with increase in c -axis length, i.e. tensile strain along the c -axis. The c -axis length was experimentally obtained from $2c \sin \theta_{(005)} = 5\lambda$ in the $2\theta-\omega$ scan of XRD where $\lambda = 1.5418 \text{ \AA}$. Except for the YBCO+BZO(8.2, 870), YBCO+BZO(8.2, 880), and YBCO+BHO(4.7, 870), the SIOV describes the $T_{c,0}$ behavior well in the fully oxidized YBCO+BMO films. Since all the fully oxidized films were cooled down under almost the same oxidation conditions, oxygen was introduced to the same level as the other fully oxidized films in the YBCO+BZO(8.2, 870), YBCO+BZO(8.2, 880), and YBCO+BHO(4.7, 870) films. Thus, one possible explanation is that T_c smaller than the T_c-c relation of the SIOV originated from compositional deviation of cations [24], not from the oxygen content. It has also been reported that T_c depended on the atomic fraction of (Ba+Zr)/Cu in Zr doped (Gd,Y)BCO tapes [25]. In the oxygen deficient films ($P_{O_2} = 5000 \text{ Pa}$ and 500 Pa), the $T_{c,0}$ agreed well with the T_c-c relation for the SIOV.

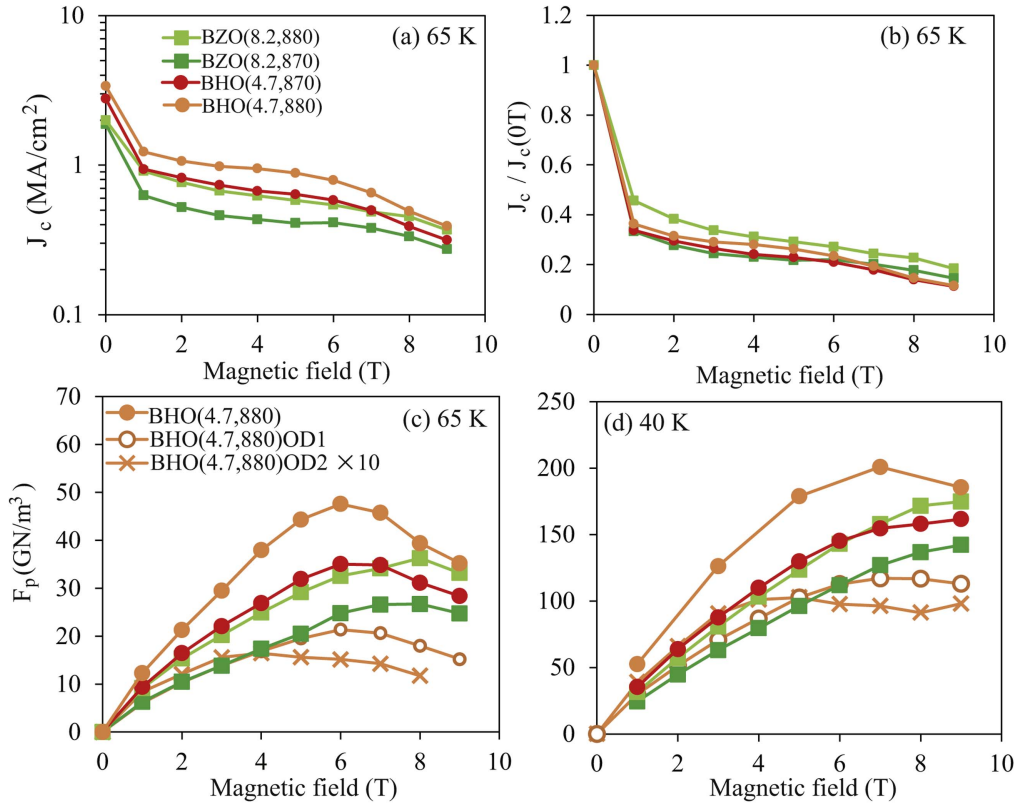


Figure 5. (a) Magnetic field dependence of (a) J_c and (b) $J_c/J_c(0\text{ T})$ at 65 K in fully oxidized films with $B_\Phi = 5\text{--}6\text{ T}$. Magnetic field dependence of F_p in fully oxidized films with $B_\Phi = 5\text{--}6\text{ T}$ and the oxygen deficient films in temperatures of (c) 65 K and (d) 40 K. The F_p for BHO(4.7, 880) OD2 is multiplied by 10.

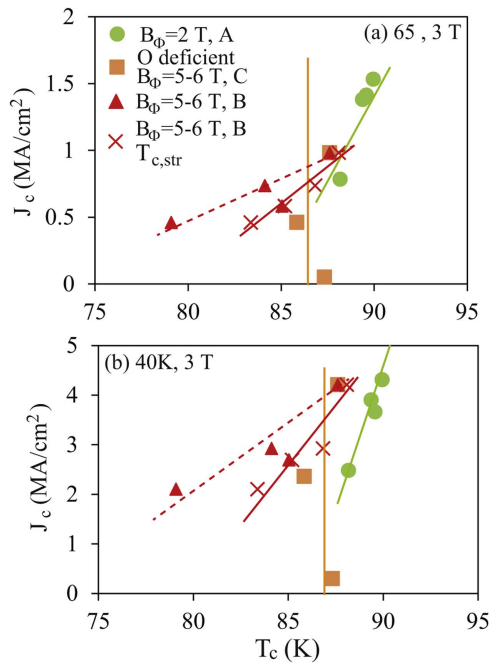


Figure 6. J_c - $T_{c,0}$ relation in a magnetic field of 3 T at (a) 65 K and (b) 40 K. The results for the fully oxidized films ($B_\Phi = 2\text{ T}$, series A), the fully oxidized films with cation compositional deviation ($B_\Phi = 5\text{--}6\text{ T}$, series B), and the oxygen deficient films ($B_\Phi = 5\text{--}6\text{ T}$, series C) are compared. J_c - $T_{c, \text{str}}$ for the series B is also shown.

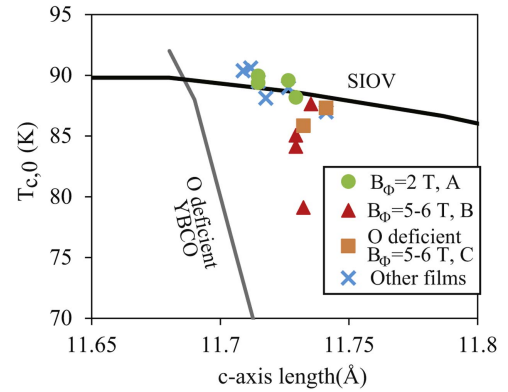


Figure 7. $T_{c,0}$ as a function of c -axis length in the films. Solid lines show the T_c estimated for the SIOV [18] and oxygen deficient YBCO bulk [16].

$\delta = \sim 0\text{--}0.3$ even at $P_{O_2} = 500\text{ Pa}$ and 5000 Pa at temperatures of $400\text{--}500^\circ\text{C}$ according to [16, 26]. $T_{c,0} = T_c(\text{SIOV})$ suggests that these cooling conditions did not degrade $T_{c,0}$ along the strongest superconducting path, but might kinetically induce oxygen inhomogeneity—specifically, oxygen deficient regions with low T_c . The films with the relation of $T_{c,0} = T_c(\text{SIOV})$, including series A, contain SIOVs; the two-step transition in series B was caused by cation compositional deviation.

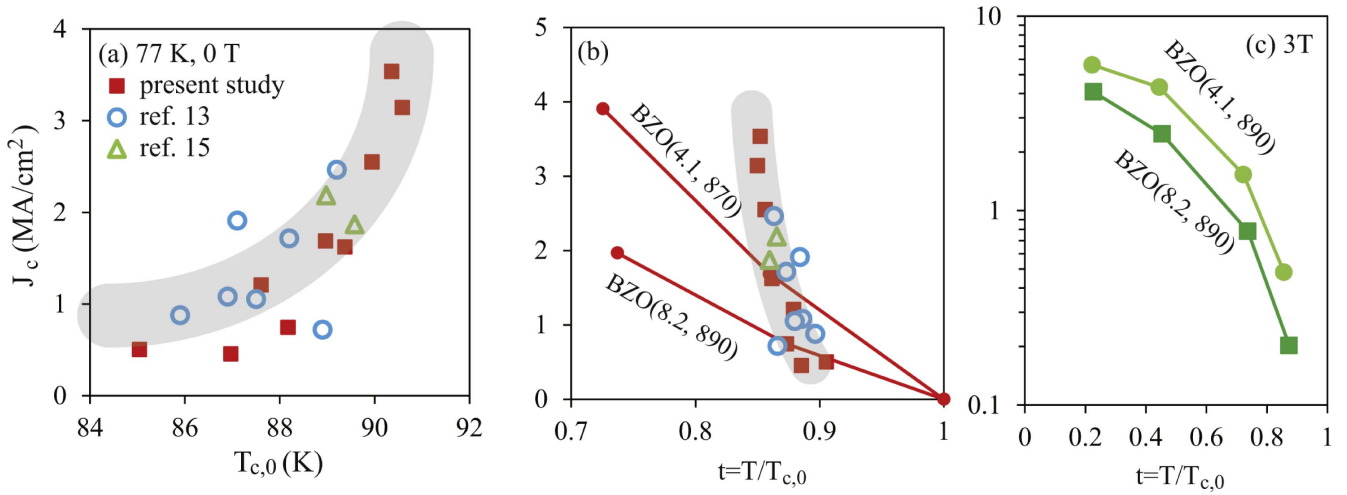


Figure 8. (a) $T_{c,0}$ dependence of J_c at 77 K at 0 T, which is compared with our previous results [13, 15]. For the present study, the data for fully oxidized YBCO+BMO films without the two-step transition is shown. (b) J_c as a function of the reduced temperature, $t = T/T_{c,0}$, which was obtained from the temperature dependence and sample dependence of J_c . In (a) and (b), the J_c in the films of [13, 15] are redefined at the same J_c criterion as the present films. (c) J_c in a magnetic field of 3 T as a function of the reduced temperature in the YBCO+BZO(4.1, 890) and YBCO+BZO(8.2, 890).

On the other hand, J_c significantly decreased with decrease in the oxygen pressure during oxidization in the series C in figure 6 although the $T_{c,0}$ was determined by the SIOV regardless of the oxygen pressure. This suggests that the J_c mechanism in the oxygen deficient films is different from that in series A and B. The T_c is determined along the strongest superconducting path, but the J_c is dependent on the effective area for current flow. Horii *et al* reported that J_c was 0.5–2.5 MA cm⁻² at a self-field in a temperature of 77 K depending on oxygen annealing conditions, although T_c was not changed by the annealing (89.2–90.2 K); the significant variation of J_c without changing T_c in the J_c – T_c relation was found to originate from inhomogeneous oxygen distribution, as confirmed by magneto-optical imaging [27]. $T_{c,0} = T_c(\text{SIOV})$ was achieved in our study only along the strongest superconducting path, but the oxygen deficient films included a large fraction of the low T_c region, which decreased the effective area and J_c . Thus, we clarified the compositional situation in the present films: fully oxidized films containing SIOVs and cation compositional deviation for BZO(8.2, 870), BZO(8.2, 880) and BHO(4.7, 870) in series B; oxygen deficient films (inhomogeneously oxidized films) for OD1 and OD2 in series C; and fully oxidized films containing SIOVs for the other films including series A and BHO(4.7, 880) in series B.

4.3. Influence of T_c on J_c

To explain the influence of T_c on J_c , figure 8(a) shows a $T_{c,0}$ dependence of $J_c(0\text{ T})$ at 77 K for the fully oxidized YBCO+BMO films without the two-step transition in the present films and the films in [13, 15]. Because the J_c at 0 T is determined by the single vortex pinning of nanorods, it can be analyzed in discussion of the T_c effect without considering the B_Φ difference. Regardless of nanorod material and matching field, the J_c at 77 K and 0 T tends to decrease with decreasing $T_{c,0}$.

J_c values at a fixed temperature are usually measured to evaluate the properties of the various samples for development of superconducting wires and tapes; therefore, the discussion of J_c at a fixed temperature is very important. However, to understand the J_c – T_c relation, the J_c should be analyzed based on the reduced temperature ($t = T/T_{c,0}$). The temperature dependence of $J_c(0\text{ T})$ in fixed samples is compared with the $(T_{c,0})$ dependence of $J_c(0\text{ T})$ on a per-sample basis in figure 8(b). It is apparent that the $J_c(0\text{ T})$ – $T/T_{c,0}$ relations obtained from the temperature dependence and sample dependence are significantly different. To compare the J_c at the same reduced temperature, J_c can be interpolated with the $J_c(0\text{ T})$ – $T/T_{c,0}$ curve. While $J_c(0\text{ T})$ is 0.74 MA cm⁻² for 77 K ($t = 0.87$) and 0.95 MA cm⁻² for $t = 0.85$ in YBCO+BZO(8.2, 890), $J_c(0\text{ T})$ is 3.1 MA cm⁻² for 77 K ($t = 0.85$) in YBCO+BSO(3.6, 880). These data indicate that the reduced temperature cannot explain the difference in $J_c(0\text{ T})$ in figure 8(a), and the influence of the reduced temperature is not so strong. In the present study, since the influence of the reduced temperature is small, the present data fully support the conclusion without detailed comparison of the $J_c(0\text{ T})$ at a fixed reduced temperature. The J_c – $T/T_{c,0}$ at 3 T is also shown in figure 8(c), indicating that the reduced temperature cannot explain the J_c difference in magnetic field either. The T_c effect on J_c is classified into two types: the first is related to the thermodynamic state, which can be discussed based on the reduced temperature; the second originates from microscopic effects related to the superconducting state, which also change T_c . The present study on J_c – $T/T_{c,0}$ cannot be explained only by the reduced temperature, and the J_c changed systematically with $T_{c,0}$. This indicates that the T_c effect on J_c in the present films is mainly caused by microscopic effects such as matrix superconductivity. The variation of structure (such as strain) and oxygen content in the matrix due to nanorod incorporation determined the T_c , and thereby the nanorod pinning strength and J_c .

The present discussion clarified that the difference in the T_c and J_c behavior between the films originated from the pinning strength and the fraction and distribution of weak superconducting regions, i.e. the cation compositional deviation and the oxygen deficiency. Based on the analysis, we obtained a J_c landscape based on geometric and compositional factors: the J_c values in the YBCO+BMO films are determined by three factors of compositional homogeneity (effective area), matching field (geometric effect), and T_c (nanorod pinning strength). These factors should be comprehensively controlled based on the J_c – T_c relation and normalized J_c – B behavior. The oxidation conditions and PLD conditions (effective area), nanorod structure including matching field (geometric factor), and strain and RE in the $\text{REBa}_2\text{Cu}_3\text{O}_{7-\delta}$ (T_c) [10, 28] should be optimized.

5. Summary

In summary, J_c – B curves were plotted to investigate the J_c mechanism in YBCO+BMO films. The influence of T_c and compositional homogeneity on J_c was separated from the effect of matching field in these YBCO+BMO films by examining the J_c – T_c relations. The normalized J_c – B behavior was shown to be altered by the matching field, and the J_c – T_c relation to depend on compositional homogeneity and T_c . The J_c values in the YBCO+BMO films were determined by the three factors of matching field (geometric effect), T_c (nanorod pinning strength), and compositional homogeneity (effective area). Thus, a J_c landscape based on geometric and compositional factors was obtained, and the importance of J_c – T_c analysis in the understanding of the J_c mechanism in YBCO+BMO films was demonstrated.

Acknowledgment

The authors would like to thank N Matsukida for helping with the TEM observation.

ORCID iDs

Tomoya Horide  <https://orcid.org/0000-0003-1753-9179>

References

- [1] Larbalestier D, Gurevich A, Feldmann D M and Polyanskii A 2001 *Nature* **414** 368
- [2] Blatter G, Geshkenbein V B and Koopmann J A G 2004 *Phys. Rev. Lett.* **92** 067009
- [3] MacManus-Driscoll J L, Foltyn S R, Jia Q X, Wang H, Serquis A, Civalé L, Maiorov B, Hawley M E, Maley M P and Peterson D E 2004 *Nat. Mater.* **3** 439
- [4] Haugan T, Barnes P N, Wheeler R, Meisenkothen F and Sumption M 2004 *Nature* **430** 867
- [5] Gutierrez J et al 2007 *Nat. Mater.* **6** 367
- [6] Maiorov B, Baily S A, Zhou H, Ugurlu O, Kennison J A, Dowden P C, Holesinger T G, Foltyn S R and Civalé L 2009 *Nat. Mater.* **8** 398
- [7] Xu A, Delgado L, Khatri N, Liu Y, Selvamanickam V, Abrahimov D, Jaroszynski J, Kametani F and Larbalestier D C 2014 *APL Mater.* **2** 046111
- [8] Rizzo F et al 2016 *APL Mater.* **4** 061101
- [9] Sieger M et al 2017 *IEEE Trans. Appl. Supercond.* **27** 6601407
- [10] Tsuchiya Y, Miura S, Awaji S, Ichino Y, Matsumoto K, Izumi T, Watanabe K and Yoshida Y 2017 *Supercond. Sci. Technol.* **30** 104004
- [11] Chen S, Sebastian M A, Gautam B, Wilt J, Chen Y, Sun L, Xing Z, Haugan T and Wu J 2017 *Supercond. Sci. Technol.* **30** 125011
- [12] Mele P, Matsumoto K, Horide T, Ichinose A, Mukaida M, Yoshida Y, Horii S and Kita R 2008 *Supercond. Sci. Technol.* **21** 032002
- [13] Horide T, Taguchi K, Matsumoto K, Matsukida N, Ishimaru M, Mele P and Kita R 2016 *Appl. Phys. Lett.* **108** 082601
- [14] Horide T, Matsumoto K, Mele P, Yoshida Y, Kita R, Horii S and Mukaida M 2009 *Phys. Rev. B* **79** 092504
- [15] Horide T, Matsukida N, Ishimaru M, Kita R, Awaji S and Matsumoto K 2017 *Appl. Phys. Lett.* **110** 052601
- [16] Jorgensen J D, Veal B W, Paulikas A P, Nowicki L J, Crabtree G W, Claus H and Kwok W K 1990 *Phys. Rev. B* **41** 1863
- [17] Cantoni C, Gao Y, Wee S H, Specht E D, Gazquez J, Meng J, Pennycook S J and Goyal A 2011 *ACS Nano* **5** 4783
- [18] Horide T, Kametani F, Yoshioka S, Kitamura T and Matsumoto K 2017 *ACS Nano* **11** 1780
- [19] Horide T and Matsumoto K 2014 *Supercond. Sci. Technol.* **27** 115013
- [20] Awaji S, Yoshida Y, Suzuki T, Watanabe K, Hikawa K, Ichino Y and Izumi T 2015 *Appl. Phys. Express* **8** 023101
- [21] Horide T, Otsubo K, Kita R, Matsukida N, Ishimaru M, Awaji S and Matsumoto K 2017 *Supercond. Sci. Technol.* **30** 074009
- [22] Talantsev E F, Stickland N M, Wimbush S C, Storey J G, Tallon J L and Long N J 2014 *Appl. Phys. Lett.* **104** 242601
- [23] Augieri A et al 2010 *J. Appl. Phys.* **108** 063906
- [24] Proyer S, Stangl E, Borz M, Hellebrand B and Bauerle D 1996 *Physica C* **257** 1
- [25] Gharahcheshmeh M H, Galstyan E, Xu A, Kukunuru J, Katta R, Zhang Y, Majkic G, Li X-F and Selvamanickam V 2017 *Supercond. Sci. Technol.* **30** 015016
- [26] Kishio K, Shimoyama J, Hasegawa T, Kitazawa K and Fueki K 1987 *Jpn. J. Appl. Phys.* **26** L1228
- [27] Horii S, Ichinose A, Mukaida M, Matsumoto K, Ohazama T, Yoshida Y, Shimoyama J and Kishio K 2004 *Jpn. J. Appl. Phys.* **43** L1223
- [28] Wee S H, Goyal A, Martin P M, Li J, Paranthaman M and Heatherly L 2006 *Supercond. Sci. Technol.* **19** L42